

Influence of the Phase Fractions on the Formation of Eutectic Colonies: A Large-Scale Phase-Field Study

Michael Kellner,* Henrik Hierl, and Britta Nestler

The growth of two-phase eutectic colonies is a frequently observed phenomenon in the microstructure of directionally solidified ternary alloys. The formation of these macroscopic structures is driven by microscopic instabilities, caused by minor component impurities, diffusing into the liquid from the two solidifying phases. Due to an accumulation of this impurity component, a morphological instability at the eutectic front leads to the formation of eutectic colonies. In this work, the phase-field method is used to investigate the influence of different melt composition and hence of the adjusting phase fractions on the growth of eutectic colonies. For this purpose, specially designed model systems, $N\text{-}x\text{A-}y\text{C}$, with defined phase fractions of the solids are generated on the basis of the high performance material NiAl-34Cr. Based on these models, the evolution of eutectic colonies is investigated in two- and three-dimensional (3D) large-scale simulations with up to $3 \cdot 10^9$ cells. To perform these highly computationally intense large-scale 3D simulations, the computational framework used is optimized in several layers. The results obtained show the influence of the melt composition on the formation and characteristics of the evolved eutectic colonies and provide new insights into the formation of these macroscopic structures.

1. Introduction

In a huge amount of alloy systems of great importance for advanced engineering materials, the solidification process involves the simultaneous formation of two or more phases from the liquid phase. During the directional solidification of eutectic multi-component alloys, the evolution of different ordered fibrous and lamellar microstructures can be observed. Besides these ordered structures, various forms of instability-driven morphologies can evolve depending on the applied composition and temperature. The growth of eutectic colonies^[1] is one of these morphological structures. These structures are mainly observed in ternary systems for alloy compositions in the vicinity of a binary eutectic reaction. Widely used and important alloys in advanced engineering applications, in which eutectic colony formation occurs, are gray and white cast iron, aluminium-silicon and aluminium copper, copper-based and steel alloys as well as nickel-based


superalloys. Based on an understanding of the underlying physical mechanisms, optimizing eutectic colony microstructures are crucial steps in the development of advanced engineering materials, allowing engineers to design materials with tailored microstructures and properties that meet the specific demands of diverse industries. The formation of eutectic colony microstructures holds importance in advanced engineering materials as they often result in enhanced mechanical properties of materials. Upon the structural characteristics, the microstructure can lead to increased hardness, strength, and toughness, making the material more suitable for demanding engineering applications. Moreover, eutectic colonies provide a means of controlling the grain size in materials and hence are a key material property to establish higher strength and fatigue resistance. In addition, certain eutectic microstructures can enhance the corrosion or heat resistance of materials as, for example, of importance in aerospace or automotive components.

The formation of eutectic colonies is driven by instabilities in the planar solidification front, caused by the rejection of the ternary impurities diffusing from the two solidifying phases into the liquid. With increasing solidification velocities, the solidification front becomes morphologically unstable and an impurity-driven Mullins–Sekerka instability^[2,3] can occur, in which parts of the front grow preferentially, resulting in a cell-like pattern with a characteristic spacing.^[4] In these cases, the evolving

M. Kellner, B. Nestler
Institute of Applied Materials
Karlsruhe Institute of Technology
Straße am Forum 7, 76131 Karlsruhe, Germany
E-mail: michael.kellner@partner.kit.edu

H. Hierl, B. Nestler
Institute of Nanotechnology
Karlsruhe Institute of Technology
Hermann-von-Helmholtz-Platz 1, 76344 Eggenstein-Leopoldshafen,
Germany

B. Nestler
Institute of Digital Materials
Karlsruhe University of Applied Science
Moltkestr. 30, 76133 Karlsruhe, Germany

 The ORCID identification number(s) for the author(s) of this article can be found under <https://doi.org/10.1002/adem.202301766>.

© 2024 The Authors. Advanced Engineering Materials published by Wiley-VCH GmbH. This is an open access article under the terms of the Creative Commons Attribution-NonCommercial-NoDerivs License, which permits use and distribution in any medium, provided the original work is properly cited, the use is non-commercial and no modifications or adaptations are made.

DOI: 10.1002/adem.202301766

morphology changes and the solidifying eutectic fibers and lamellae devolve not only along the direction of the temperature gradient, but also tilt to the growth direction. Due to the tilting, a curved solidification front is established that extends the lamellar spacing. Eventually this leads to the growth of new lamellae, to establish a reduced spacing, following the Jackson–Hunt criterion.^[5] Also caused by tilting, the fibers or lamellae start to grow against each other, forming interfaces between the colonies. Each colony consists of multiple splitting events of fibers or lamellae that are many times smaller than the colony itself. Similar to eutectic, dendritic, and cellular structures, the size of a colony depends on its growth rate^[6] and thus on the temperature gradient. With increasing velocity, more and similarly sized colonies evolve, while with decreasing velocity the size distribution of the colonies is larger and fewer colonies are found.

The formation of eutectic colonies is experimentally investigated by Raj et al.^[6] for the system Ni–Al–Cr–Mo, by Durand et al. for the systems MnSb–(Sb,Bi) and MnSb–(Sb,Sn)^[7] and by Hecht et al.^[8] for the system Al–Ag–Cu. Theoretical work on the growth behavior of eutectic colonies are published by Himemiya^[9] and by Plapp and Karma.^[10] The later ones continued their theoretical work^[10] by comparing it with 2D large-scale simulations of the system Al–Ag–Cu, using an isotropic phase-field model.^[11] This model is extended by Lahiri and Choudhury^[12] to study the effect of the growth fronts in multiphase alloys, by considering the anisotropy of the solid–solid and solid–liquid interfaces. This results in a fixed colony spacing evolves in their simulations, which is not observed for isotropic systems. Depending on the growth velocity and the cell spacing, Lan and co-workers^[13–16] classify different shapes of the colony formation within phase-field simulation studies. Spiral dendrites, a special arrangement of eutectic colonies, are also investigated with the phase-field method by Pusztai, Ratkai, and co-workers^[17,18] as well as Akamatsu et al.^[19,20]

Some recent studies of the eutectic colony formation, performed with the phase-field method, have been published by the authors themselves.^[21,22] In^[21] the influence of the applied temperature gradient and in^[22] additionally, the influence of the growth velocity on the evolving eutectic colonies is studied in two-dimensional (2D) large-scale simulations of the system NiAl–34Cr. As the formation of eutectic colonies requires the occurrence of new lamellae within the simulation domain, a kinetically consistent concentration-driven nucleation mechanism is introduced in^[21] which follows the approach from Schoof et al.^[23] for martensitic phase transformation. Other nucleation mechanisms are presented by Böttger et al.^[24] and Nestler and Wheeler.^[25] A summary of the work on the study of nucleation mechanisms, using the phase-field method, can be found in Podmaniczky et al.^[26]

Continuing the work of^[21,22] this article investigates influence of the melt compositions and subsequently the influence of the phase fractions on the eutectic colony formation. Preliminary studies on these investigations are presented in^[27,28] In order to simulate the nucleation during directional solidification in the eutectic and three off-eutectic compositions, the nucleation mechanism from^[21] is transferred to the system AlCu–5Ag in^[27] For each composition, a stable set of parameters is found to perform isothermal Jackson–Hunt studies^[5] in 2D simulations. Unfortunately, by increasing the simulation domain, a stable

configuration of the nucleation parameters is not found to establish the growth of eutectic colonies for the system AlCu–5Ag. Hence, the investigation of the eutectic colony formation is initially continued on the basis of the previously used system NiAl–34Cr, which was originally derived in [29] for the phase-field simulation of the direction solidification process. For this purpose, the Gibbs energy functions of the system NiAl–34Cr are recalculated by using the thermodynamic database of Peng et al.^[30] and the approximation workflow of Dargahi Noubary et al.^[31] To investigate the influence of the melt composition on the formation of eutectic colonies, the next step is to modify the newly modeled Gibbs energy paraboloid of the liquid phase of NiAl–34Cr to shift the position of the equilibrium composition of the liquid. New eutectic material systems N–xAl–yCr are digitally designed by consequently adjusting the melt compositions in the simulation domain. This approach is in contrast to other works,^[27,32,33] which also investigates the influence of the melt composition on the adjusting microstructures. In these works, only the melt compositions in the simulation domains are varied, resulting in off-eutectic simulations. The additional modifications of the Gibbs energy paraboloid in the work presented here still describes eutectic systems, which increases the stability of the simulated microstructures. These newly designed eutectic material systems do not represent the original NiAl–34Cr system. However, using the system NiAl–34Cr as basis of the modeling ensures the thermodynamic consistency of the new designed N–xAl–yCr systems.

The results of preliminary studies for the material systems N–37.7A–24.0C, N–33.3A–34.0C, and N–28.9A–44.0C, in small 2D simulation domains of 1500 × 1000 cells, are summarized in^[28] Based on these preliminary study results, four newly developed material systems, namely N–28.4A–45.3C, N–31.7A–37.8C, N–33.3A–34.0C, and N–31.7A–34.0C, are selected for the upcoming investigations in this work, so as to achieve phase ratios from 50:50 to 66:33, for the solid phases after the solidification. To enable the growth of multiple coexisting colonies within one simulation, 2D and 3D large scale simulations are performed on the gauss centre of supercomputer high performance computing (GCS HPC)-system SUPERMUC-NG at the Leibniz Supercomputing Centre^[34] by using an optimized and vectorized solver within the massively parallel multiphysics framework PACE3D.^[35,36] The simulation results are compared visually and by analyzing the evolving structures with respect to the size and growth height of the evolving colonies.

The so-called eutectic reactions occur at specific compositions and temperature conditions, resulting in the formation of eutectic and in particular eutectic colony microstructures. Widely used and important alloys in advanced engineering applications, in which eutectic colony formation occurs, are gray and white cast iron, aluminium–silicon and aluminium copper, copper-based and steel alloys as well as nickel-based superalloys. Based on an understanding of the underlying physical mechanisms, optimizing eutectic colony microstructures are crucial steps in the development of advanced engineering materials, allowing engineers to design materials with tailored microstructures and properties that meet the specific demands of diverse industries. The formation of eutectic colony microstructures holds importance in advanced engineering materials as they often result in enhanced mechanical properties of materials.

Upon the structural characteristics, the microstructure can lead to increased hardness, strength, and toughness, making the material more suitable for demanding engineering applications. Moreover, eutectic colonies provide a means of controlling the grain size in materials and hence are a key material property to establish higher strength and fatigue resistance. In addition, certain eutectic microstructures can enhance the corrosion or heat resistance of materials as, for example, of importance in aerospace or automotive components.

In the following, the basic phase-field model is introduced together with the implemented nucleation mechanism and the optimizations made. Subsequently, the modelling of the four newly developed material systems is presented in detail, the 2D and 3D simulation setups are described, and the applied analysis method based on a watershed algorithm is explained. Based on this, the simulation results are shown and the influence of the melt composition on the evolving 2D and 3D structures is investigated. Finally, the results are summarized and discussed.

2. Phase-Field Model

For the simulations of the eutectic colony formation within the ternary model systems N-xA-yC, a thermodynamically consistent phase-field model, based on a grand potential functional and an Allen-Cahn-type variation, is used.^[37–39] The $N=3$ order parameters $\phi_{\hat{\alpha}}$, describe the local phase fractions of the three phases participating in the eutectic reaction $Liq \rightleftharpoons B2 + A2$ in N-xA-yC. To differentiate the phases α, β, \dots from their indices, the indices are marked by an $\hat{\square}$ symbol in the following equations. The development of the N phase fields $\phi_{\hat{\alpha}}$ are described by the time evolution equations

$$\tau \varepsilon \frac{\partial \phi_{\hat{\alpha}}}{\partial t} = -\varepsilon \left(\underbrace{\frac{\partial a(\phi, \nabla \phi)}{\partial \phi_{\hat{\alpha}}}}_{:=rhs_{1,\hat{\alpha}}} - \nabla \cdot \underbrace{\frac{\partial a(\phi, \nabla \phi)}{\partial \nabla \phi_{\hat{\alpha}}}}_{:=rhs_{2,\hat{\alpha}}} \right) - \frac{1}{\varepsilon} \frac{\partial \omega(\phi)}{\partial \phi_{\hat{\alpha}}} - \underbrace{\frac{\partial \psi(\phi, \mathbf{\mu}, T)}{\partial \phi_{\hat{\alpha}}}}_{:=rhs_{2,\hat{\alpha}}} - \frac{1}{N} \sum_{\hat{\beta}=1}^N \underbrace{(rhs_{1,\hat{\beta}} + rhs_{2,\hat{\beta}})}_{:=\Lambda} \quad (1)$$

to couple the different timescales of the evolution equations, the relaxation parameter τ is introduced.^[38] The width of the interface between the phases is controlled by the parameter ε and its shape is modeled by the gradient energy $a(\phi, \nabla \phi)$ and by the obstacle potential $\omega(\phi)$. The gradient energy density $a(\phi, \nabla \phi)$ is described in^[39] and includes the interface energies $\gamma_{\hat{\alpha}\hat{\beta}}$ and the function $a_c(\tilde{q})$, which describes the anisotropy in the interface energies. In this work, isotropic interface energies are used to model the system N-xA-yC, leading to the function $a_c(\tilde{q}) = 1$. The formulation of the obstacle potential $\omega(\phi)$ is also given in [39]. Besides the interfacial energies $\gamma_{\hat{\alpha}\hat{\beta}}$, the obstacle potential also includes the higher order term $\gamma_{\alpha\beta\delta}$, which is introduced to reflect the correct equilibrium angle conditions at the triple junctions,^[39,40] by suppressing the appearance of a third phase at the phase boundaries. The driving forces for the phase transitions are described by the differences of the grand potentials $\psi_{\hat{\beta}}$, which are stored in the grand potential function $\psi(\phi, \mathbf{\mu}, T)$. The

derivation of the grand potentials from thermodynamic CALPHAD databases is discussed in detail in the chapter 4. Finally, the Lagrange multiplier Λ is introduced to fulfill the constraint $\sum_{\hat{\alpha}=1}^N \partial \phi_{\hat{\alpha}} / \partial t = 0$.

To enable the growth of new nuclei in the simulations, a noise term ζ_{α} of the form

$$\zeta_{\alpha} = \begin{cases} n_{\text{dist}} \cdot A & \forall \phi_{\beta} \phi_l > 0 \quad t_{\text{step}} \bmod i = 0 \\ 0, & \text{else} \end{cases} \quad (2)$$

is added to the right hand side of the phase-field evolution equation,^[21,27] where n_{dist} is the noise function and t_{step} is the time step of the simulation. For the conducted material system, the nucleation can be adjusted for the conducted material system by means of the limit c_{dev} , the amplitude A and the interval i . The limit c_{dev} describes the deviation of the concentrations from the initially set melt composition. If the concentration of one or more components reaches this predefined limit c_{dev} in the interface region ahead of the solidification front, the nucleation mechanism is executed. The strength of the nucleation is adjusted by the amplitude A and the interval step i defines time period in which the criterion c_{dev} must be tested.

To ensure mass conservation during the simulations, the time evolution of the chemical potentials is introduced and coupled with the evolution equation of the phase fields. The vector of the chemical potential $\mathbf{\mu}$ consists of a parameter μ_k for each component ($k = N, A, C$), and its time evolution is derived from the mass balance of the $K=3$ concentrations and Fick's law as

$$\frac{\partial \mathbf{\mu}}{\partial t} = \left[\sum_{\hat{\alpha}=1}^N h_{\hat{\alpha}}(\phi) \left(\frac{\partial c_{\hat{\alpha}}(\mathbf{\mu}, T)}{\partial \mathbf{\mu}} \right) \right]^{-1} \times \left(\nabla \cdot (M(\phi, \mathbf{\mu}, T) \nabla \mathbf{\mu} - J_{\text{at}}(\phi, \mathbf{\mu}, T)) - \sum_{\hat{\alpha}=1}^N c_{\hat{\alpha}}(\mathbf{\mu}, T) \frac{\partial h_{\hat{\alpha}}(\phi)}{\partial t} - \sum_{\hat{\alpha}=1}^N h_{\hat{\alpha}}(\phi) \left(\frac{\partial c_{\hat{\alpha}}(\mathbf{\mu}, T)}{\partial T} \right) \frac{\partial T}{\partial t} \right) \quad (3)$$

here, the vectors $c_{\hat{\alpha}}(\mathbf{\mu}, T)$ contain the concentrations $A_{c_{\hat{\alpha}}}, C_{c_{\hat{\alpha}}}$ and $N_{c_{\hat{\alpha}}}$ for the considered phase $\hat{\alpha}$. The mobility term $M(\phi, \mathbf{\mu}, T)$ ^[38] contains the diffusion coefficient matrix \mathbf{D} of the phases involved and the function $h_{\hat{\alpha}}$ is introduced in the form $h_{\hat{\alpha}} = \phi_{\hat{\alpha}}^2(3 - 2\phi_{\hat{\alpha}})$ to interpolate between the different phases. The term J_{at} is an anti-trapping current,^[38,41,42] used to balance the effects of artificially enlarged interfaces from phase-field modeling.

The evolution of the temperature is described by a moving analytic approach of the form

$$\frac{\partial T}{\partial t} = \frac{\partial}{\partial t} (T_0 + G(y - v_G t)) = -Gv_G \quad (4)$$

starting from an initially imprinted temperature field, with the base temperature T_0 , the temperature T evolves, with the gradient G and the velocity v_G in the growth direction y .

3. Simulation Setup and Model Optimizations

The focus of this work is on the numerical study of the evolution of eutectic colonies with the phase-field method in 2D and 3D

simulation domains. For this, 2D and 3D Bridgman-type furnace setups are used.^[21,43] Starting from an initial arrangement of nuclei on one side of the simulation domain, the two solid phases A2 and B2 evolve into a liquid domain, controlled by the applied temperature gradient (Equation 4) in the γ -direction (z -direction in 3D) and at the velocity v . An infinite domain, perpendicular to the solidification front, is modeled by periodic boundary conditions and a constant flux of the melt into the domain is realized by a Dirichlet boundary condition at the liquid end of the domain. At the opposite solid end of the domain, a no-flux boundary condition is applied. Illustrations of the 2D and 3D simulation domains are given in,^[21,44] respectively.

To ensure the comparability of the resulting microstructures, each simulation type (2D or 3D) is performed with the same thermal gradient G and the same velocity v_G . The simulation values and their physical equivalence are summarized in Table B1 of the Appendix B. Also the random Voronoi tessellation used to generate the initial arrangement of nuclei at the beginning of the simulation has been generated only once for the 2D and for the 3D simulations in advance and is used in all simulations of each type, respectively.

The initially investigated 2D simulations are performed for 6 million time steps in a simulation domain of 4000×750 cells, on the SUPERMUC-NG with 96 cores. Due to the used optimized moving-window technique,^[45] the finally resulting structures reach a final size of approximately 4000×6000 cells. The subsequently performed 3D simulations are performed in a domain of $2000 \times 2000 \times 750$ cells with 18 432 cores for 4 million time steps. Since the maximum usable time step width dt depends on the dimension of the simulations, dt is reduced by 35% for the 3D simulations compared to the 2D simulation. To compensate for this smaller time step width as well as the reduced calculation time the growth velocity of the structures in the 3D simulations is enlarged by increasing the temperature gradient velocity by 20%. It is mentioning that already nonphysically enlarged growth velocities are used for the 2D simulations to reduce the computational cost of achieving adequate growth heights. A further increase in speed is not used, as this affects the stability of the simulations. The 3D microstructures reach a final height of up to 3000 cells. The individual parameters for the 2D and 3D simulations are also given in Table B.1.

To resolve the different scales between the eutectic and the colony structures simultaneously in one simulation, large simulation domains with a high resolution are required. Again, simulating of such large domain sizes with more than $1000 \times 1000 \times 500$ voxel cells in a reasonable time (<several days) requires an execution of the simulations with more than 10.000 cores^[39,46] and thus using the fastest supercomputers currently available.

To increase the efficiency of these computations, compared to the previously published simulation results of eutectic colonies in 2D,^[21] an optimized and vectorized version of the solver is implemented in the massively parallel multiphysics framework PACE3D^[36] version 2.5.1. The optimizations in this new solver are based on the improvements introduced by Bauer et al.^[47] and Hötzer et al.^[39] for the computation of directional solidification with the phase-field method within the massively parallel HPC framework WALBERLA (www.walberla.net). These improvements affect different layers of the code implementation, mainly for the

kernels of the phase fields $\phi_{\hat{\alpha}}$ and the chemical potentials μ_i , which account for more than 90% of the total program runtime.^[47] For example, the number of computationally intensive divisions is reduced by using lookup tables and multiplications with the inverse instead. Additionally, inverse square root calculations, required for vector normalizations, are replaced by approximated values provided by a fast inverse square root algorithm.^[48] Next, explicit single instruction multiple data (SIMD) vectorization is included in both computation kernels. Since the targeted architectures all have a vector width of four values with double precision, a straightforward method is used for vectorizing the algorithm of the μ -kernel by unrolling the innermost loop and updating four cells in one iteration. In contrast to the work of Bauer et al.^[47] and Hötzer et al.^[39] the number of used components is variable and not limited to three. The number of performed calculation loops of the μ -kernel is updated with the required number of investigated components.

For the ϕ -kernel, a more natural approach is used. Instead of dealing with four cells simultaneously, four phases are represented with the SIMD vector. Thus, the phase field is still updated cellwise, allowing branching on a cell-by-cell basis. However, a significant speed-up of the kernels is achieved, since some computationally intensive terms only have to be calculated for certain cell configurations.^[47]

To further use the potential of vector and matrix calculations to reduce the computational effort, the formulations of the Gibbs energies are also converted into a vector/matrix notation. Instead of using the approximated parabolic formulations of

$$g_{\hat{\alpha}}(c, T) = \sum_{i=1}^K i A_{\hat{\alpha}}^i(T) i c^2 + \sum_{j=1}^K j B_{\hat{\alpha}}^j(T) j c + C_{\hat{\alpha}}(T) \quad (5)$$

with the temperature dependent coefficients $A_{\hat{\alpha}}^i(T)$, $B_{\hat{\alpha}}^j(T)$, and $C_{\hat{\alpha}}(T)$ and the bulk concentration vector \mathbf{c} , for the observed ternary systems, the following matrix notation

$$g_{\hat{\alpha}}(\mathbf{c}, T) = \langle \mathbf{c}, \Xi_{\hat{\alpha}}(T) \mathbf{c} \rangle + \langle \mathbf{c}, \xi_{\hat{\alpha}}(T) \rangle + X_{\hat{\alpha}}(T) \quad (6)$$

with the matrix $\Xi_{\hat{\alpha}}(T)$, the vector $\xi_{\hat{\alpha}}(T)$ and the scalar $X_{\hat{\alpha}}(T)$, which are defined as

$$\Xi_{\hat{\alpha}}(T) = \begin{bmatrix} {}^1A_{\hat{\alpha}}(T) + {}^3A_{\hat{\alpha}}(T) & {}^3A_{\hat{\alpha}}(T) \\ {}^3A_{\hat{\alpha}}(T) & {}^2A_{\hat{\alpha}}(T) + {}^3A_{\hat{\alpha}}(T) \end{bmatrix} \quad (7)$$

$$\xi_{\hat{\alpha}}(T) = \begin{bmatrix} {}^1B_{\hat{\alpha}}(T) - {}^2A_{\hat{\alpha}}(T) + {}^3B_{\hat{\alpha}}(T) \\ {}^2B_{\hat{\alpha}}(T) - {}^2A_{\hat{\alpha}}(T) + {}^3B_{\hat{\alpha}}(T) \end{bmatrix} \quad (8)$$

$$X_{\hat{\alpha}}(T) = C_{\hat{\alpha}}(T) + {}^3A_{\hat{\alpha}}(T) + {}^3B_{\hat{\alpha}}(T) \quad (9)$$

is implemented following.^[39]

In addition to the improvements from,^[39,47] efficient buffering techniques are used for expensive computations such as the calculation of the fluxes. As additional optimizations, the patterns in the update rule for the phase field are exploited to reduce the number of computational instructions, and the temperature field is specified in a unidirectional functional. By reducing the call frequency of the moving-window technique^[45] a further reduction in the global communication is achieved.

4. Modeling of Thermodynamic Gibbs Energy Densities

The used ternary model systems N-xA-yC are derived based on the thermodynamic information stored in the thermodynamic CALPHAD database of Peng et al.^[30] for the system Ni-Al-Cr-Mo. This database also contains the Gibbs energy information of the ternary system Ni-Al-Cr and improves the database from^[49] with more recent experimental data in the vicinity of the eutectic reaction of the ternary system. To extract the data from,^[30] the workflow of Dargahi Noubary et al.^[31] is used. In this semi-automated workflow, the equilibrium concentrations of the evolved phases are first calculated for a given temperature by using the software package THERMOCALC.^[50] For a melt concentration of 34.4 at% Al, 34.0 at% Cr, and 31.6 at% Ni, corresponding to the eutectic composition of the system NiAl-34Cr and an isothermal undercooling temperature T_{isoth} of 1710 K the results of this equilibrium calculation are summarized in **Table 1**.

Next, the Gibbs energies for the phases *A2*, *B2*, and *Liq* are calculated at T_{isoth} with THERMOCALC in a range around their equilibrium concentrations and approximated by using a least square method and second-order concentration dependent polynomials of the form as in Equation 5. After a small adaption of the parameters $B_{\alpha}^j(T)$ and $C_{\alpha}^j(T)$, to improve the accordance of the equilibrium concentrations, the adjusted Gibbs energy functions are reduced to two components by using the constraint $N_{C_{\alpha}} = 1 - A_{C_{\alpha}} - C_{C_{\alpha}}$. The reduced functions are subsequently transferred to the used matrix notation from Equation (6), to derive the following dimensionless Gibbs energy formulations

$$g_{A2}^{\text{eut}}(A_c, C_c) = (A_c, C_c) \begin{bmatrix} 3.293 & 1.750 \\ 1.750 & 1.549 \end{bmatrix} \begin{pmatrix} A_c \\ C_c \end{pmatrix} + (A_c, C_c) \begin{bmatrix} -3.798 \\ -2.423 \end{bmatrix} + 0.033 J_{\text{sim}} \text{ cells}^{-3} \quad (10)$$

$$g_{B2}^{\text{eut}}(A_c, C_c) = (A_c, C_c) \begin{bmatrix} 3.878 & 1.956 \\ 1.956 & 1.898 \end{bmatrix} \begin{pmatrix} A_c \\ C_c \end{pmatrix} + (A_c, C_c) \begin{bmatrix} -3.922 \\ -1.498 \end{bmatrix} - 0.488 J_{\text{sim}} \text{ cells}^{-3} \quad (11)$$

and

Table 1. Equilibrium concentrations of *A2* and *B2* for an undercooling temperature T_{isoth} of 1710 K and the concentration of *Liq* for the eutectic reaction at $T_{\text{eut}} = 1718.47$ K, calculated on the basis of. [30]. All entries are rounded after the second decimal place.

Phase name	Temp. in [K]	$A_{C_{\alpha}, \text{equi}}$ in [at%]	$C_{C_{\alpha}, \text{equi}}$ in [at%]	$N_{C_{\alpha}, \text{equi}}$ in [at%]
<i>A2</i>	$T_{\text{isoth}} = 1710$	12.81	82.96	4.23
<i>B2</i>	$T_{\text{isoth}} = 1710$	46.03	7.69	46.28
<i>Liq</i>	$T_{\text{eut}} = 1718.47$	34.40	34.00	31.60

$$g_{\text{Liq}}^{\text{eut}}(A_c, C_c, T) = (A_c, C_c) \begin{bmatrix} 1.800 & 0.823 \\ 0.823 & 0.578 \end{bmatrix} \begin{pmatrix} A_c \\ C_c \end{pmatrix} + (A_c, C_c) \begin{bmatrix} -1.810 \\ -0.347 \end{bmatrix} - 0.755 T - 0.252 J_{\text{sim}} \text{ cells}^{-3} \quad (12)$$

for the observed phases *A2*, *B2*, and *Liq*, respectively. To reduce the computational effort, only the concentration-independent parameter $C_{\text{Liq}}(T)$ of the *Liq* phase is defined as temperature-dependent. The temperature dependence is modeled such that the grand potential differences between the liquid and the solid phase is zero at the eutectic temperature. As a result, there is no driving force between the phases at T_{eut} .

Despite a wide variation of the parameters A , I , and c_{dev} to adjust the nucleation mechanism, as well as of the isothermal undercooling temperature T_{isoth} and the solidification velocity v , no stable growth of eutectic colonies was established using these approximated Gibbs energy functions. This may be due to the fact that the concentration accumulations ahead of the solidification fronts do not form properly. Because of this, either the nucleation mechanism is too weak, resulting in a stable planar eutectic solidification front or the nucleation mechanism is too strong, resulting in an unstable interface between the phases.

The concentration accumulations ahead of the solidification front can be increased by specifically adjusting the applied melt composition in the simulations. However, a straightforward change of the melt concentration, how it is done for example in,^[27,32,33] results in an off-eutectic composition, which has an influence on the stability of the systems. Therefore, instead of just changing the melt concentration, the entire Gibbs energy paraboloid of the liquid phase is modified to shift the position of the equilibrium composition of the liquid. To do this, the parameters $B_{\alpha}^j(T)$ and $C_{\alpha}^j(T)$ of Equation (5) are adjusted to satisfy the equilibrium conditions and to map the correct Gibbs energies for the equilibrium concentrations. An additional adjustment of the melt composition to the modeled Gibbs energy function generates new eutectic material systems.

These new material systems do not represent the original NiAl-34Cr system and are hereafter referred to as N-xA-yC, where N is the original Ni concentration, A is Al and C is Cr. The variables x and y in N-xA-yC respectively describe the amounts of A and C in at% in the current system. The evolving N- and A-rich (or Ni- and Al-rich) phase is still labeled as *B2*, while the C-rich (or Cr-rich) phase is labeled as *A2*.

For the upcoming studies, four newly designed systems are selected, namely N-28.4A-45.3C, N-31.7A-37.8C, N-33.3A-34.0C, and N-31.7A-34.0C. The newly modelled Gibbs energy functions of the liquid paraboloids for these systems are given in the Equation (A.1)–(A.4) in the Appendix A, respectively. In **Figure 1**, the melt compositions of these systems are marked in the original liquidus projection of NiAl-34Cr, derived from the database of Peng et al.^[30] The melt compositions of all systems are located slightly beside the tie line between the equilibrium concentrations of the two solid phases (dashed green line in Figure 1), with a higher amount of N. In addition, all compositions also show a deviation from the eutectic line of the liquidus

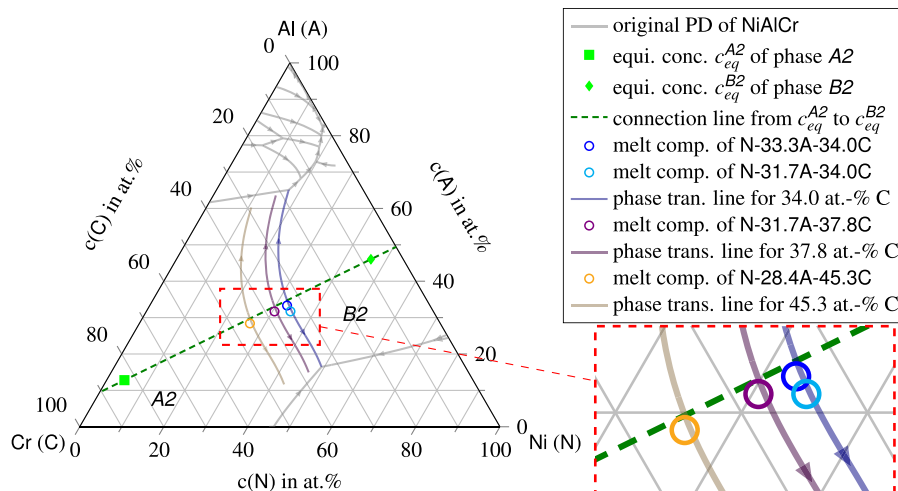


Figure 1. Illustration of melt compositions for the systems: N-28.4A-45.3C, N-31.7A-37.8C, N-33.3A-34.0C, and N-31.7A-34.0C, within the liquidus projection of NiAl-34Cr, derived from the database of Peng et al.^[30] The newly modeled transition lines for the different systems are highlighted in blue, violet, and orange, respectively.

projection to a higher amount of C. Both deviations should result in a favored growth of the C-rich (originally Cr-rich) phase A2.

The systems N-33.3A-34.0C, N-31.7A-37.8C, and N-28.4A-45.3C are selected to illustrate the influence of the phase fractions on the microstructure evolution. Based on the equilibrium concentrations of the solids and the respective liquid phase of these three systems, the lever rule for the phases A2 and B2 results in phase ratios of 33:66, 40:60, and 50:50. As shown in the highlighted enlargement beneath the legend of Figure 1, the melt composition of the system N-31.7A-34.0C (marked in cyan) has a larger deviation from the equilibrium line compared to the other three systems. For this system, the lever rule predicts the same phase fraction of 33:66, for A2 and B2, as for the system N-33.3A-34.0C. By comparing the simulation results for the systems N-33.3A-34.0C and N-31.7A-34.0C, the influence of the deviation from the tie line on the evolving eutectic colony structures is investigated. By modeling new eutectic systems instead of only changing the melt composition, the influence of off-eutectic melt compositions on the formation of the eutectic colonies can be neglected and the formation is only depending on the evolving phase fractions and the deviation from the tie line.

5. Analysis Methods

To determine microstructure characteristics of the eutectic colonies obtained by 2D and 3D phase-field simulations, a workflow of data analysis steps is established. With this workflow, contiguous regions of each colonies are detected and labeled. These labeled areas are then further analyzed in terms of number, height, and size. For this purpose, the first step is to calculate a height map of the solidified structure based on the isolines of the diffuse solid-liquid interface. Due to the different growth heights of the two solid phases the solidification front does not have a smooth surface. To reduce the impact of the different growth heights, the 0.1 isoline of the liquid phase is chosen for the height map generation, instead of the more common

0.5 isoline. Then, a watershed segmentation algorithm^[51–53] is applied to the height map to divide the solidification front into different sections. However, several deviations and disturbances remain in the front, which initially leads to an over-segmentation of the structures. To solve this problem, an optimization loop is applied to merge several sections based on a predefined criterion. For this purpose, the maximum height h_{\max} of the detected sections are stored and sorted in a list. Starting from the section with the lowest height, the direct neighborhood of the corresponding section is identified and the maximum height of all contact points cp_{\max} with neighboring sections is detected. If the difference d in height between this contact point cp_{\max} and the maximum height h_{\max} of the section is less than a predefined criterion d_{crit} , the section with the lower maximum height is merged with the neighboring section, by relabeling it with the index of the remaining section. This process is continued up to the section with the overall highest maximum point. With this the number of detected section can be reduced by multiple magnitudes. Based on these finally detected sections, the geometries of the colonies are analyzed in 2D and 3D.

The criterion d_{crit} for the merging of sections, is validated in the upcoming investigation of the 2D simulations, since the number of colonies in these simulations is usually clearly to decide. For this purpose, the criterion is increased in full integer steps starting from one, until the detected number of colonies matches the visually observed number of colonies. The same criterion d_{crit} is subsequently used to validate the 3D simulations, where a visual detection is mostly not uniquely possible.

6. Results

6.1. Influence of Melt Composition on 2D Eutectic Colony Formation

Using a highly optimized and vectorized solver within the PACE3D framework, 2D simulations are performed on the high

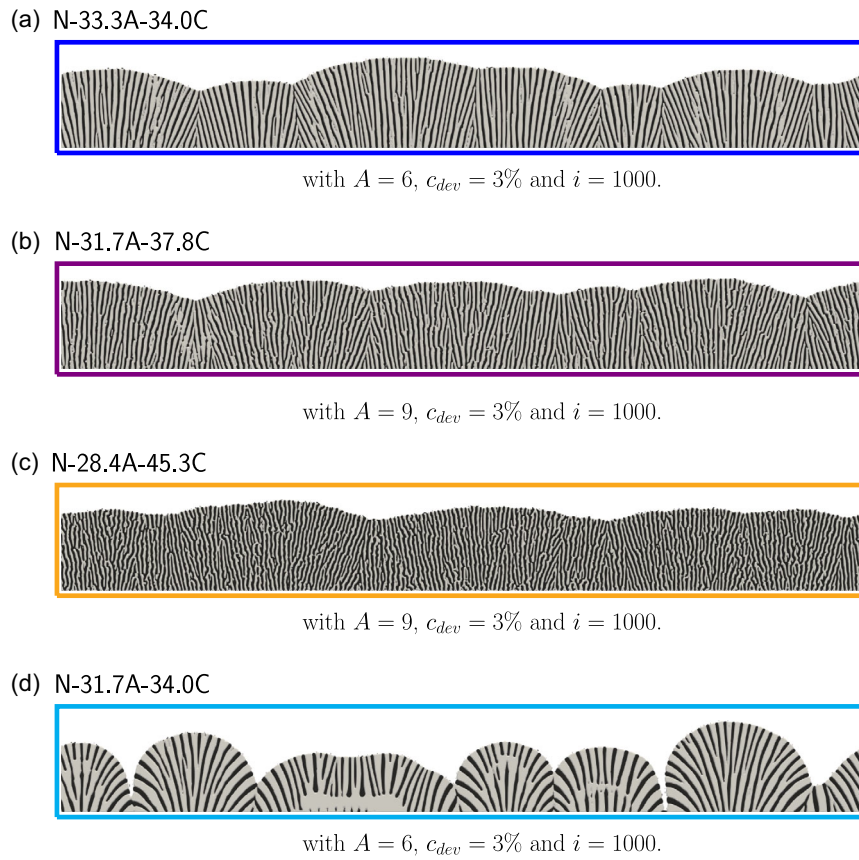


Figure 2. Comparison of the two-dimensional simulation results for the systems: a) N-33.3A-34.0C, b) N-31.7A-37.8C, c) N-28.4A-45.3C, and d) N-31.7A-34.0C, showing the formation of eutectic colonies with different eutectic spacings and colony shapes. The used parameters (amplitude A , limit c_{dev} , and interval i) for the nucleation mechanism are given below the microstructures.

performance computing cluster SUPERMUC-NG, to validate the stability of the selected systems and to adjust the applied nucleation mechanism and the described watershed-based analysis method. **Figure 2** shows the simulation results with the best aligned and distinguishable colonies for each system. The configuration parameters of the nucleation mechanism used for the simulations (amplitude A , limit c_{dev} , and interval i) are listed in the subfigures and differ only in the amount of the amplitude A .

With a lower proportion of component A and an increasing proportion of component C, a refinement of the eutectic structure (Figure 2a–c) can be seen. Accompanying this trend, the colony boundaries are less pronounced for finer eutectic lamellar spacings. The finest structure with a composition of N-28.4A-45.3C resembles a seaweed structure. It can also be seen that the roughness of the entire solidification front decreases with a finer inner eutectic structure.

All plots in Figure 2 show the growth of eutectic colonies, with the colonies in the microstructure of N-31.7A-34.0C in Figure 2d being the most pronounced. Another striking feature within the microstructures is also found in the simulation results of N-31.7A-34.0C. Areas of pure B2 phase (grey) can be seen in the centering three colonies. At these points the growth of the A2-fibers is interrupted. Such a microstructure feature was not observed in the microstructures of the other simulations.

One reason for this peculiarity in the microstructure of N-31.7A-34.0C can be found in the large deviation from the tie line for this system. This can lead to a larger fluctuation in the concentration ahead of the solidification front can occur. Again, these fluctuations can lead to an overgrowth of the A2-fibers and thus to an establishment of areas with pure B2-matrix phase. However, as these fluctuations are not permanent, new A2 fibers nucleate and the familiar lamellar structure within the colonies is continued.

To analyze the 2D colonies, the 0.1 isoline of the liquid phase is plotted in **Figure 3**, for each simulation. Based on these isolines, which represent the profiles of the solidification fronts, the involved eutectic colonies are determined using the watershed-based analysis described in chapter 5. The colored regions in the subfigures a–d show the detected sections of colonies for a criterion d_{crit} of seven grid cells. The criterion $d_{crit} = 7$ is chosen in accordance with the visual observation of the colony boundaries in the 2D simulations. The same choice of d_{crit} is used for the analysis of the 3D structures, as this is the smallest criterion that leads to a match between the determined and visually observed colony numbers.

The initially found maximum and minimum heights in the solidification front are reduced on the basis of the determined colony sections. In the profiles in Figure 3, the remaining

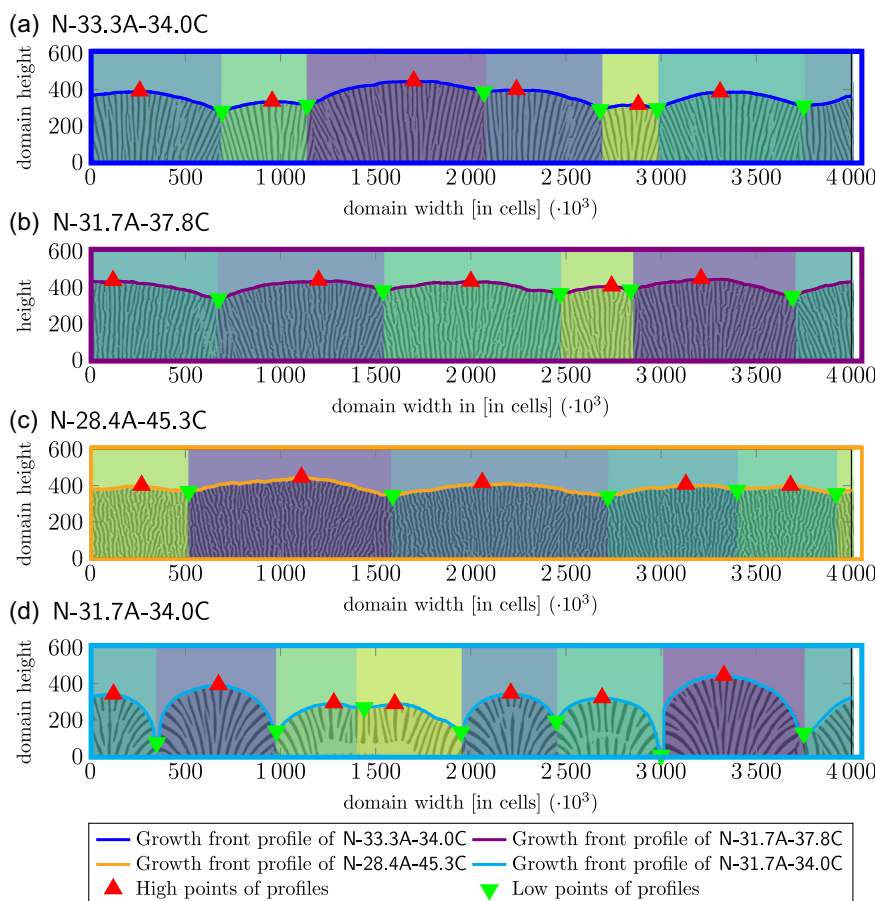


Figure 3. Visualization of the solidification front profiles for the systems: a) N-33.3A-34.0C, b) N-31.7A-37.8C, c) N-28.4A-45.3C after 6 million time steps, and d) N-31.7A-34.0C after 3.6 million time steps with high Δ and low points ∇ , which are used to measure the colony geometries and the event of disruption to the overall solidification front. The colored regions illustrate the detected sections of eutectic colonies from the presented analysis.

extreme points are marked at the with the symbols Δ and ∇ , respectively. The geometries of the colonies are calculated on the basis of the detected sections as well as these extreme points. The height of a colony h_{colony}^{2D} in 2D is defined by the average deviation in height (y -direction) between its maximum point and its two neighboring minimum points, while the width of a colony λ_{colony} is defined by the distances of the neighboring minimum points in the x -direction. In contrast to the described detection of the height map in chapter 5, the 0.5 isoline is used to calculate the height and width of the colonies. For all colonies within the simulations, **Table 2** summarizes the averaged results of these geometry measures along with the measured phase fractions

Table 2. Analysis of 2D eutectic colony simulations.

Name of simulation	Time step for analysis	Phase fraction ratio of A2:B2	$\lambda_{\text{eut}}^{2D}$ in cells	$\lambda_{\text{colony}}^{2D}$ in cells	h_{colony}^{2D} in cells
N-33.3A-34.0C	$6 \cdot 10^6$	34.6: 65.4	27 ± 14	666 ± 368	63 ± 42
N-31.7A-37.8C	$6 \cdot 10^6$	39.5: 60.5	24 ± 17	800 ± 430	65 ± 38
N-28.4A-45.3C	$6 \cdot 10^6$	49.5: 50.5	20 ± 18	800 ± 338	53 ± 32
N-31.7A-34.0C	$3.6 \cdot 10^6$	34.2: 65.8	42 ± 38	571 ± 279	210 ± 167

and lamellar spacings $\lambda_{\text{eut}}^{2D}$ of the eutectic structure. It has to be mentioned that the microstructures of the systems are not converged. Due to the continuously active nucleation mechanism, steady instabilities can occur at the solidification front, which lead to an ongoing transformation of the microstructures. Therefore, all results shown in Table 2 reflect the growth states presented here.

As expected from the lever rule, the microstructures of the first three systems N-33.3A-34.0C, N-31.7A-37.8C, and N-28.4A-45.3C respectively show phase proportions of approximately 33:66, 40:60, and 50:50 for the phases A2 and B2. The colony heights h_{colony}^{2D} are evaluated as the average difference in the maximum (Δ) and minimum (∇) front positions and a decrease in the maximum colony heights is found with decreasing lamellar eutectic spacings, i.e., decreasing differences in the phase fractions of the solids. A similar behavior can be stated for the number of evolved colonies within the considered simulation domain. While the microstructure of the system N-33.3A-34.0C in Figure 3a indicates the growth of six colonies within the simulation domain, only five colonies are detected in the simulations of the systems N-31.7A-37.8C and N-28.4A-45.3C, as shown in Figure 3b,c. Consequently, as the number of colonies within

the simulation domain decreases, the average colony width $\lambda_{\text{colony}}^{2D}$ is increasing. Regardless of the detected colony numbers within the simulation, the maximum deviations from the average colony width are between 42% and 55% of the detected colony width $\lambda_{\text{colony}}^{2D}$. This ratio is detected for all investigated simulations, which indicates a more or less homogeneous size distribution of the evolved colonies.

The analysis of the simulations for the systems N-33.3A-34.0C, N-31.7A-37.8C, and N-28.4A-45.3C show that a reduction in the concentration of A, in favor of C, yields 1) a decreasing difference in the phase fractions between the two solid phases; 2) less colonies with less pronounced characteristics such as maximum and minimum colony heights; and 3) less curvature along the solidification front. The visual detection of the boundary regions between the colonies and of the colonies themselves is also de-emphasized from N-33.3A-34.0C in Figure 2a to N-28.4A-45.3C in Figure 2c. A similar behavior is also found in a preliminary study in smaller simulation domains of 1500×1000 ^[28] for the systems N-37.7A-24.0C, N-33.3A-34.0C, and N-28.9A-44.0C, referred to as AB-24.0E, AB-34.0E, and AB-44.0E, respectively. In this study, less pronounced eutectic colonies are also observed for the simulation of the system AB-24.0E, with a phase fraction difference of around 80:20, compared to N-33.3A-34.0C (or AB-34.0E in [28]). In summary, it can be said that larger deviations in the phase proportions of the two solidifying phases favor the growth of eutectic colonies in 2D.

This conclusion is confirmed by the simulation results for N-31.7A-34.0C, shown in Figure 2d and Figure 3d, with a phase fraction of about 33:66, but with a larger deviation from the tie line. The evolved microstructure shows the formation of seven well-defined colonies with strongly curved solidification fronts, with the colonies on the domain width between 980 and 1950 (see Figure 3d) cells just split up into two separate colonies, reducing the colony spacing. The height of the colonies are four to five times greater than in the other three simulations and the variation in the average colony height is four times greater. The curvatures in the solidification fronts are so strong that the applied moving-window technique^[45] has almost shifted the delimitation areas between the colonies out of the domain so that the residual fluid remains between the colonies. The simulation is terminated after 3.6 million time steps. By comparing the simulation results of the systems N-33.3A-34.0C and N-31.7A-34.0C in Figure 2a,d and their solidification front profiles in Figure 3a,d, respectively, it can be assumed that the properties of the eutectic colonies become more prominent with larger deviations from the tie line.

To complete the investigations of the 2D simulations, a brief discussion of the underlying eutectic structures follows. The lamellar spacings λ_{eut} of the eutectic structures are measured by counting the number of A2 rods within the solidified microstructures along the *x*-direction of the entire simulation domain and dividing the width of the solidification domain by this counted number. The results are also given in Table 2. While the microstructures of the systems N-33.3A-34.0C, N-31.7A-37.8C, and N-28.4A-45.3C show lamellar spacings λ_{eut} of a similar order of magnitude with a trend to smaller spacings with decreasing phase fractions, the lamellar spacing in the microstructure of the system N-31.7A-34.0C is approximately

twice as large as in the other three systems. This again results from the larger deviation from the tie line of this system. Using the same initial parameters for the temperature profile, the microstructures of the systems N-33.3A-34.0C, N-31.7A-37.8C, and N-28.4A-45.3C grow with similar growth velocities v_F . However, due to the larger deviation from the tie line, a reduced growth velocity of the solidification front by 27% is established within the simulations of the system N-31.7A-34.0C, which leads to a larger lamellar spacing.^[5]

6.2. Influence of Melt Composition on 3D Eutectic Colony Formation

Subsequently, 3D large-scale simulations of a domains with $2000 \times 2000 \times 750$ cells are performed on the high-performance computing cluster SUPERMUC-NG with 18 432 cores. The resulting microstructures after 4 million time steps are shown in Figure 4 and their respective solidification fronts in Figure 5. For each system, the growth of two elongated clusters of colonies with well-pronounced boundary regions between them is observed. These delimitation areas are located at similar positions within the microstructure and are a result of the initial start settings. To achieve a better comparability of the resulting structures, the same Voronoi tessellation is used to set the initial seeds. This leads to the same initial setup for all 3D simulations and hence to the establishment of similar boundary regions between the two elongated colonies. However, the formation of colony clusters has not been observed in large-scale 2D simulations so far and is therefore a new discovery based on 3D investigations. Unfortunately, due to the limited number of detected clusters within the simulations a quantitative analysis of their properties is not yet meaningful.

By analyzing the phase proportions, different values are found, as expected for the adjusting underlying lamellar microstructures of the four investigated systems. This can be clearly seen in the top views of the microstructures in Figure 5. The measured values of the phase proportions are summarized in Table 3 and show a good accordance with the results of the 2D simulations and the expected values from the lever rule. The widths of the lamella pairs are measured in a similar way to the 2D simulations, but in four cuts through the simulation domain, in the *x*-direction and in the *y*-direction, respectively. The distance between these cuts is 500 cells. The averaged results for all eight cuts are summarized in Table 3 and show a similar trend as the 2D simulations. However, the actually measured values are approximately 24–66% higher. This increase is a result of the spatial lamellar structure, that evolves in the 3D simulation. Since the growing lamellae are not aligned, the performed cuts are not directed perpendicular to the orientations of the lamellae. Therefore, the measured values do not represent the exact values of the lamellar widths and are referred to below as w_{eut}^{3D} , instead of $\lambda_{\text{eut}}^{3D}$. However, the measured values are still valid for a qualitative comparison of the lamellar spacings of the 3D microstructures.

Compared to 2D simulations, similar but less pronounced tendencies in the eutectic colony formation can be visually observed in 3D simulations. The clarity of the colony cluster manifestation increases with greater differences in the phase fractions (compare subfigures a–c in Figure 4 and 5) and with a greater

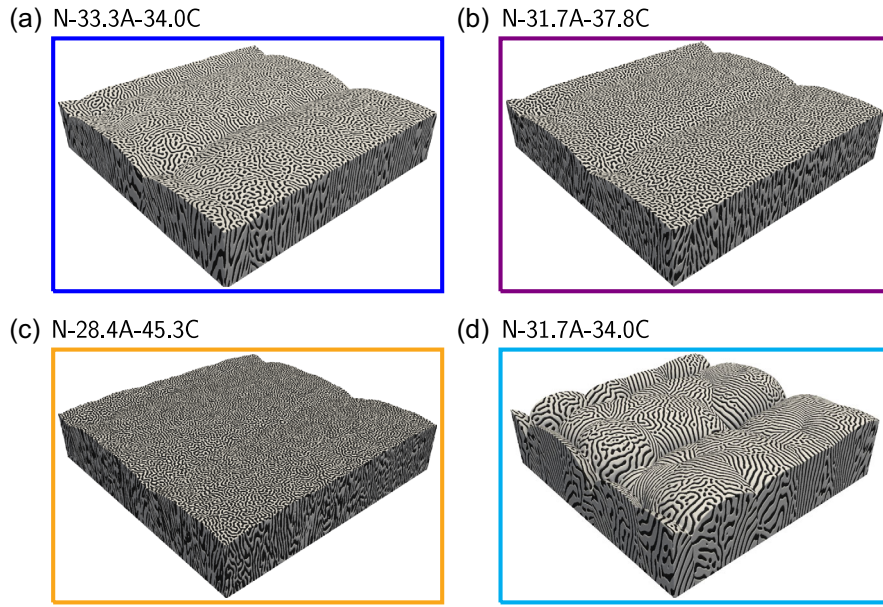


Figure 4. Comparison of the 3D simulation results for the systems: a) N-33.3A-34.0C, b) N-31.7A-37.8C, c) N-28.4A-45.3C, and d) N-31.7A-34.0C showing the formation of eutectic colonies.

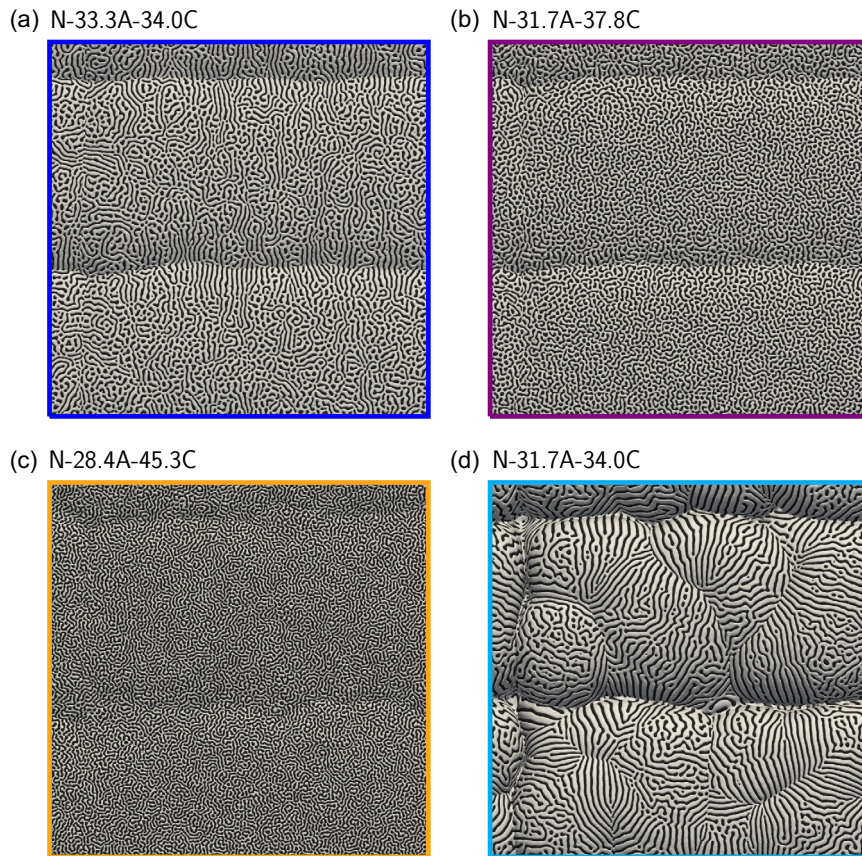


Figure 5. Comparison of the solidification fronts from 3D simulations of the systems: a) N-33.3A-34.0C, b) N-31.7A-37.8C, c) N-28.4A-45.3C, and d) N-31.7A-34.0C, showing the formation of eutectic colonies.

Table 3. Analysis of eutectic clusters in 3D simulations.

Name of simulation	Phase proportions ratio of A2:B2	w_{cut}^{3D} av. in cells
N-33.3A-34.0C	34.1: 65.9	45±158
N-31.7A-37.8C	39.2: 60.8	35±106
N-28.4A-45.3C	49.4: 50.6	27±61
N-31.7A-34.0C	33.5: 66.5	52±207

deviation from the tie line (compare subfigures (a) and (d) in Figure 4 and 5).

The geometries of the colonies in the 3D simulations are validated similarly to the 2D simulations, by using the watershed-based analysis with a criterion $d_{crit} = 7$. The results of the colony detection are illustrated in the **Figure 6–9** next to the top views of their corresponding microstructure. At first sight, the clusters in the microstructures of the systems N-33.3A-34.0C, N-31.7A-37.8C, and N-28.4A-45.3C have an almost uniform surface, with two prominent horizontal valleys (Figure 5a–c), while in N-31.7A-34.0C several well-defined colonies are observed within the clusters (Figure 5d). This can be seen in particular in the changes in

the alignments of the evolved lamellar structures, as shown in the top view of the microstructure in Figure 5d. The pattern formation is purely driven by diffusion and no anisotropy is used in the simulations, which could also lead to the formation of differently aligned structures. However, the quantitative analysis of the 3D structures prove that the clusters of the systems N-33.3A-34.0C, N-31.7A-37.8C, and N-28.4A-45.3C in the Figure 6–8 also include multiple colonies. The detected colonies are colored according to the given legends and are numbered from the colony with the highest maximum to the colony with the lowest maximum. In particular, a good agreement with the visually observed colonies is obtained for the microstructure of system N-31.7A-34.0C in Figure 9, which show the formation of six eutectic colonies. The analysis also convincingly shows the microstructure properties of the other alloy compositions (At this point the authors refer to the additionally provided videos of the 3D structures).

In contrast to the 2D microstructures, the number of colonies does not consequently decrease with smaller differences in the phase fractions of the solids. While the microstructures of the systems N-33.3A-34.0C and N-31.7A-37.8C in the Figure 6 and 7 have five and four colonies, respectively, eight colonies

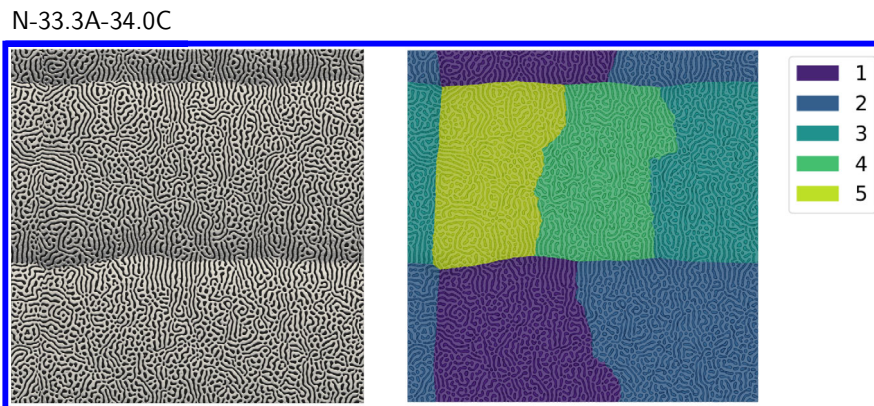


Figure 6. Comparison of the solidification front from 3D simulations of the systems: N-33.3A-34.0C, with a colored map of the detected colonies within the structure.

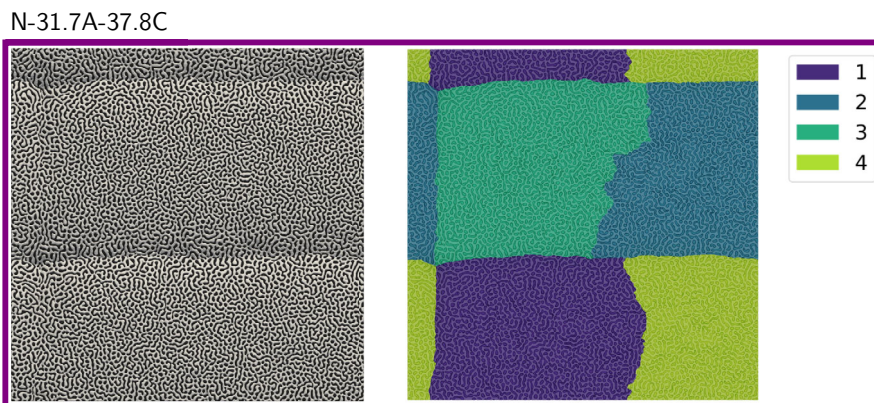


Figure 7. Comparison of the solidification front from 3D simulations of the systems N-31.7A-37.8C, with a colored map of the detected colonies within the structure.

N-28.4A-45.3C

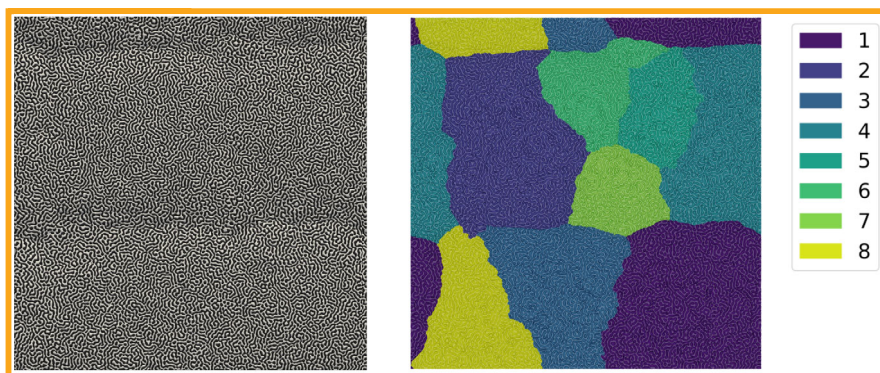


Figure 8. Comparison of the solidification front from 3D simulations of the systems N-28.4A-45.3C, with a colored map of the detected colonies within the structure.

N-31.7A-34.0C

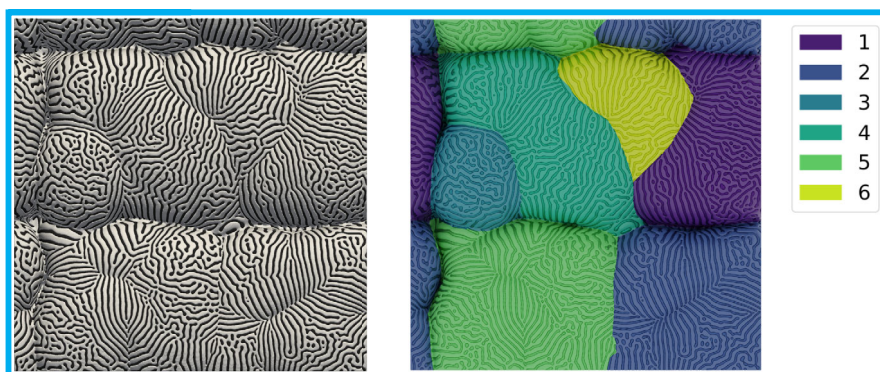


Figure 9. Comparison of the solidification front from 3D simulations of the systems N-31.7A-34.0C, with a colored map of the detected colonies within the structure.

are detected in the microstructure of system N-28.4A-45.3C in Figure 8 with the smallest difference in the phase proportions. Even when changing the criterion d_{crit} of the watershed-based analysis to larger values, the number of detected colonies remains larger for N-28.4A-45.3C, compared to N-33.3A-34.0C and N-31.7A-37.8C. A reason for this can be found in the underlying lamellar microstructures of the three systems. While N-28.4A-45.3C shows a less aligned microstructure than N-33.3A-34.0C and N-31.7A-37.8C, more instabilities can occur in the solidification front. This is approved by the profiles of the 2D simulations in the Figure 2 and 3. As the microstructure has more freedom to grow in 3D, these instabilities have a better chance to form an individual colony, compared to the 2D settings.

The average sizes of the colonies A_{colony}^{3D} are given in Table 4, by measuring the number of cells covered by the colonies. Moreover, their diameters $\text{dia}_{\text{colony}}^{3D}$ are calculated by relating their corresponding measured area to a circle. The diameters are calculated to allow a better comparison of the colony sizes in 3D with the previously presented results from 2D simulations. Both values reflect the already detected number of evolving

Table 4. Analysis of eutectic colony and cluster sizes.

Name of simulation	Number of colonies	Colony sizes		
		av. A_{colony}^{3D} in cells ²	av. $\text{dia}_{\text{colony}}^{3D}$ in cells	Variation of A_{cluster} in %
N-33.3A-34.0C	5	800000 ± 273743	1005 ± 167	1.14
N-31.7A-37.8C	4	1000000 ± 152109	1128 ± 85	0.11
N-28.4A-45.3C	8	500000 ± 412384	774 ± 305	2.51
N-31.7A-34.0C	6	666666 ± 404153	897 ± 319	0.50

colonies within the simulation domain. However, the microstructure of N-28.4A-45.3C not only evolve with the greatest number of colonies, it also shows the greatest variation in the measured colony sizes and thus diameters. Due to the greater spatial freedom in 3D simulations, larger diameters $\text{dia}_{\text{colony}}^{3D}$ result for the eutectic colonies in 3D, compared to the colony widths $\lambda_{\text{colony}}^{2D}$ in 2D. Since all 3D microstructures exhibit two elongated eutectic clusters within the domain size of $2000 \times 2000 \times 750$, the average area of a cluster results in

Table 5. Analysis of eutectic colony and cluster heights.

Name of simulation	Colony heights		
	$h_{\text{colony}}^{3\text{D},\text{total}}$ in cells	$h_{\text{colony}}^{3\text{D},\text{cluster}}$ in cells	h_{cluster} in cells
N-33.3A-34.0C	72 ± 93	10 ± 5	115 ± 25
N-31.7A-37.8C	50 ± 42	9 ± 1	107 ± 2
N-28.4A-45.3C	44 ± 48	18 ± 16	90 ± 17
N-31.7A-34.0C	186 ± 333	58 ± 36	367 ± 488

2 million cells and their average width is 1000 cells. To compare their sizes, only the deviation from these area sizes are given in Table 4 whereby, the largest deviation is rediscovered for the system N-28.4A-45.3C.

The height of a 3D colony is calculated from the difference between its highest point and the maximum height of its contact areas. For each system different heights are determined and summarized in **Table 5**. Taking into account the contact areas with all other colonies, $h_{\text{colony}}^{3\text{D},\text{total}}$ represents the height of the colonies in the total domain. In contrast, $h_{\text{colony}}^{3\text{D},\text{cluster}}$ represents the colony height within the cluster by considering only contact areas with colonies from the same cluster and h_{cluster} indicated the height of the clusters themselves by summarizing the colonies of one cluster and comparing the maximum height of the entire cluster only with contact areas of colonies from the other cluster. Since only the maximum heights of the contact areas are considered for the calculations, the values in Table 5 represents the average minimum height of a colony compared to the contact areas to its neighbors.

While the tendencies for $h_{\text{colony}}^{3\text{D},\text{total}}$ and h_{cluster} are similar to the measurements in 2D, the colony height within the cluster $h_{\text{colony}}^{3\text{D},\text{cluster}}$ of N-28.4A-45.3C grows about twice as high, compared to N-33.3A-34.0C and N-31.7A-37.8C. These measurements make clear that not only do more colonies solidify in N-28.4A-45.3C compared to the other two systems, the evolving colonies are also more pronounced. As expected from the visual observations, the microstructure of the system N-31.7A-34.0C shows the largest values for all three calculated height parameters. To substantiate the observations from the investigation of the system N-31.7A-34.0C, further simulations of systems with larger and smaller deviations of the melt composition from the tie line between the phases would be required. Since these calculations are very computationally intensive, no further simulations are performed for this work. However, new insights into the formation of eutectic colonies, for example, the formation of colony clusters, are already provided by the 2D and 3D simulation results presented here. The observations made are summarized in the next chapter.

7. Conclusion

In this work, the influence of different melt compositions and consequently of different phase fractions on the formation of eutectic colonies is investigated in large-scale phase-field simulations using the high-performance microstructure simulation

framework PACE3D. For this purpose, four newly designed model systems N-xA-yC with different compositions are modeled on the basis of the well-known and investigated system NiAl-34Cr. Three of these systems N-28.4A-45.3C, N-31.7A-37.8C, and N-33.3A-34.0C are arranged along the tie line between the equilibrium concentrations of the solids. The last system N-31.7A-34.0C is constructed with a larger deviation from this tie line. By using a concentration-driven nucleation mechanism, the evolution of eutectic colonies is simulated in 2D and 3D simulation domains. The colonies are quantitatively analyzed by measuring their number, size, and height by means of a newly introduced watershed-based analysis method. The following interactions are found as results: 1) The used watershed method to detect colonies within the simulation domain has proven its suitability for the validation of the performed simulations. By using this method, instead of a purely visual detection by optical impressions, an analytical and numerical-based detection and visualization of the evolving colonies can be installed. However, for small colony heights, the method is still sensitive to the used adjustment parameters. Thus, a more unique and clearer criterion for the determination of a eutectic colony is required to increase the clarity of the results. 2) The simulation results for the systems N-28.4A-45.3C, N-31.7A-37.8C, and N-33.3A-34.0C show similar and reversed trends in the 2D and 3D simulations. While visual observation shows a concordance of the trend toward a higher clarity of colony manifestation and larger colony heights, with increasing differences in the phase proportions, the quantitative analysis of the 3D simulations proves that the visually observed 3D colonies are in fact clusters of several colonies. Within these clusters, no clear trends for the number of evolving colonies and their heights depending on the adjusting phase proportions are observed. 3) The formation of clusters including multiple colonies is first observed in 3D simulations. Such clustering has not yet been detected in 2D simulations and shows the added value for the investigation of eutectic colonies by 3D simulations. 4) Assuming the variation in the measurements, the largest total colony heights for the three systems N-28.4A-45.3C, N-31.7A-37.8C, and N-33.3A-34.0C are found in the simulations of the system N-33.3A-34.0C in both 2D and 3D. However, if only the colony heights within a cluster are considered, N-28.4A-45.3C has greater heights in 3D than N-31.7A-37.8C and N-33.3A-34.0C. Furthermore, N-33.3A-34.0C forms the largest number of evolving colonies, with a phase fraction of the solidified phases A2 and B2 of approximately 33:66. In contrast, N-28.4A-45.3C, with similar phase fractions, includes the most detected colonies in 3D. This result can be explained by the larger number of instabilities occurring in the solidification front of N-28.4A-45.3C. In 2D, these microstructure disturbances do not lead to the establishment of further colonies. More colonies are detected in 3D, due to the greater freedom of growth. Although, the colonies in N-28.4A-45.3C also show higher heights in the clusters, the cluster manifestation itself is not as clear as in N-31.7A-37.8C and N-33.3A-34.0C. 5) The most pronounced colonies are investigated in both 2D as well as 3D simulations for the system N-31.7A-34.0C, with a phase fraction of the solids of 33:66, but with a larger deviation from the tie line between the two solids. The colony heights in N-31.7A-34.0C are more than three times greater, compared

to the other simulations. Apart from the 3D computations of N-28.4A-45.3C, the simulations of N-31.7A-34.0C provide the largest number of detected colonies. Thus, it can be concluded that the deviation from the equilibrium line has a greater influence on the formation of eutectic colonies than the resulting phase fractions.

More detailed and systematic studies of eutectic colony formation in 3D are planned in forthcoming research, which require further optimizations of the model and the numerical solution scheme. Possible topics of these investigations are the influence of different process conditions on colony formation and the influence of fluid flow in the melt. The transformation into other realistic material models is also of particular interest.

Appendix A. Modeled Gibbs energy functions of the liquid phase

The Gibbs energy formulations of the *Liq* phases for the systems N-33.3A-34.0C, N-31.7A-37.8C, and N-28.4A-45.3C are derived according to the descriptions in chapter 4. The functions are written in the matrix notation used by the implementation.

$$g_{\text{Liq}}^{N-33.3A-34.0C}(A_c, C_c, T) = (A_c, C_c) \begin{bmatrix} 1.800 & 0.823 \\ 0.823 & 0.578 \end{bmatrix} \begin{pmatrix} A_c \\ C_c \end{pmatrix} + (A_c, C_c) \begin{bmatrix} -1.809 \\ -0.346 \end{bmatrix} - 0.755 T - 0.252 J_{\text{sim}} \text{ cells}^{-3} \quad (\text{A1})$$

$$g_{\text{Liq}}^{N-31.7A-37.8C}(A_c, C_c, T) = (A_c, C_c) \begin{bmatrix} 1.800 & 0.823 \\ 0.823 & 0.578 \end{bmatrix} \begin{pmatrix} A_c \\ C_c \end{pmatrix} + (A_c, C_c) \begin{bmatrix} -1.814 \\ -0.364 \end{bmatrix} - 0.755 T - 0.244 J_{\text{sim}} \text{ cells}^{-3} \quad (\text{A2})$$

$$g_{\text{Liq}}^{N-28.4A-45.3C}(A_c, C_c, T) = (A_c, C_c) \begin{bmatrix} 1.800 & 0.823 \\ 0.823 & 0.578 \end{bmatrix} \begin{pmatrix} A_c \\ C_c \end{pmatrix} + (A_c, C_c) \begin{bmatrix} -1.818 \\ -0.397 \end{bmatrix} - 0.755 T - 0.229 J_{\text{sim}} \text{ cells}^{-3} \quad (\text{A3})$$

$$g_{\text{Liq}}^{N-31.7A-34.0C}(A_c, C_c, T) = (A_c, C_c) \begin{bmatrix} 1.800 & 0.823 \\ 0.823 & 0.578 \end{bmatrix} \begin{pmatrix} A_c \\ C_c \end{pmatrix} + (A_c, C_c) \begin{bmatrix} -1.751 \\ -0.320 \end{bmatrix} - 0.755 T - 0.280 J_{\text{sim}} \text{ cells}^{-3} \quad (\text{A4})$$

Appendix B. Parameter sets for simulations

In addition to the already described parameters from the manuscript, Table B.1 also contains the numerical parameters dx and

Table B1. Summary of numerical and material parameters in dimensionless simulation parameters and in their physical units for the designed model system N-xA-yC.

General parameter set		
Parameter	Simulation value	Physical value
dx	1.0	$1.5 \times 10^{-8} \text{ m}$
ϵ	4.0	$7.5 \times 10^{-8} \text{ m}$
$\gamma_{A2-B2}, \gamma_{B2-A2}$	0.0133	2.0 J m^{-2}
$\gamma_{A2-Liq}, \gamma_{Liq-A2}$	0.0160	2.5 J m^{-2}
$\gamma_{B2-Liq}, \gamma_{Liq-B2}$	0.0133	2.0 J m^{-2}
$\gamma_{\alpha\beta\delta}$	15γ	–
T_{eut}	1.0	1718.47 K
∇T	8.73×10^{-7}	100 K mm^{-1}
for 2D simulations		
dt	1.0	$4.0 \times 10^{-8} \text{ s}$
$\tau_{A2-B2}, \tau_{B2-A2}$	5.929	–
$\tau_{A2-Liq}, \tau_{Liq-A2}$	2.686	–
$\tau_{B2-Liq}, \tau_{Liq-B2}$	4.422	–
D^{Liq}	0.18	$1.0125 \times 10^{-9} \text{ m}^2 \text{ s}^{-1}$
$D^{A2,B2}$	0	$0 \text{ m}^2 \text{ s}^{-1}$
ν_G	8.88×10^{-4}	1200 mm s^{-1}
for 3D simulations		
dt	1.0	$2.6 \times 10^{-8} \text{ s}$
$\tau_{A2-B2}, \tau_{B2-A2}$	9.122	–
$\tau_{A2-Liq}, \tau_{Liq-A2}$	4.132	–
$\tau_{B2-Liq}, \tau_{Liq-B2}$	6.803	–
D^{Liq}	0.117	$1.0125 \times 10^{-9} \text{ m}^2 \text{ s}^{-1}$
$D^{A2,B2}$	0	$0 \text{ m}^2 \text{ s}^{-1}$
ν_G	6.98×10^{-4}	1450 mm s^{-1}

dt , which each describe the size of a simulation cell or the incremental time step width for the calculations, respectively. Due to the dimensional dependence of the maximum incremental time step width, separate values for dt are used for the 2D and 3D simulations, which also leads to different actually calculated dimensionless diffusion coefficients D and relaxation parameters τ for both types of simulation setups. As solid–solid interactions are not considered in this work, the diffusion coefficients of the components in the solid phases $D^{A2,B2}$ are set to zero, which leads to a further reduction of the computational effort. To further decrease the required computational resources, a single value D^{Liq} is used for the diffusion coefficients of the components in the melt. The values for the relaxation parameters τ are calculated according to^[38] and the values for the surface tensions between the individual phases $\gamma_{\alpha-\beta}$ are the same as in.^[21]

Supporting Information

Supporting Information is available from the Wiley Online Library or from the author.

Acknowledgements

The authors gratefully acknowledge the Gauss Centre for Supercomputing e.V. (<https://www.gauss-centre.eu/>) for funding this project by providing computing time on the GCS Supercomputer SuperMUC-NG at Leibniz Supercomputing Centre (<https://www.lrz.de/>). This work has been supported by the Science Data Center “MoMaF”, also funded by the Ministry of Baden-Württemberg and the “Future Field” project “ACDC” of the strategy of excellence of the Karlsruhe Institute of Technology (KIT). Code optimizations of the simulation package PACE3D and the implementation of the colonies detection were prepared with the support of the KNMFi initiative of the Helmholtz Association within the MSE program no. 43.31.01. Special thanks goes to Marco Seiz and Leon Geisen, for the helpful discussions and their support.

Open Access funding enabled and organized by Projekt DEAL.

Conflict of Interest

The authors declare no conflict of interest.

Data Availability Statement

Research data are not shared.

Keywords

directional solidification, high performance computing, large-scale simulations, nucleation, ternary eutectic system, two- and three-dimensional simulations

Received: October 25, 2023

Revised: January 23, 2024

Published online:

-
- [1] A. Karma, M. Plapp, *JOM* **2004**, 56, 28.
 [2] W. W. Mullins, R. F. Sekerka, *J. Appl. Phys.* **1964**, 35, 444.
 [3] R. Sekerka, *J. Cryst. Growth* **1968**, 3, 71.
 [4] S. Akamatsu, G. Faivre, *Phys. Rev. E* **2000**, 61, 3757.
 [5] K. Jackson, J. Hunt, *Trans. Met. Soc. AIME* **1966**, 236, 1129.
 [6] S. Raj, I. Locci, *Intermetallics* **2001**, 9, 217.
 [7] M. Durand-Charre, F. Durand, *J. Cryst. Growth* **1972**, 13, 747.
 [8] U. Hecht, V. Witusiewicz, A. Drevermann, *IOP Conf. Ser. Mater. Sci. Eng.* **2012**, 27, 012029.
 [9] T. Himemiya, *Mater. Trans. JIM* **1999**, 40, 675.
 [10] M. Plapp, A. Karma, *Phys. Rev. E* **1999**, 60, 6865.
 [11] M. Plapp, A. Karma, *Phys. Rev. E* **2002**, 66, 061608.
 [12] A. Lahiri, A. Choudhury, *Trans. Indian Inst. Met.* **2015**, 68, 1053.
 [13] C. Lan, Y. Chang, *J. Cryst. Growth* **2003**, 250, 525.
 [14] C. Lan, C. Shih, W. Hsu, *J. Cryst. Growth* **2004**, 264, 379.
 [15] C. Lan, C. Shih, M. Lee, *Acta Mater.* **2005**, 53, 2285.
 [16] C. Lan, M. Lee, M. Chuang, C. Shih, *J. Cryst. Growth* **2006**, 295, 202.
 [17] T. Pusztai, L. Rátkai, A. Szállás, L. Gránásy, *Phys. Rev. E* **2013**, 87, 032401.
 [18] L. Rátkai, A. Szállás, T. Pusztai, T. Mohri, L. Gránásy, *J. Chem. Phys.* **2015**, 142, 154501.
 [19] S. Akamatsu, M. Perrut, S. Bottin-Rousseau, G. Faivre, *Phys. Rev. Lett.* **2010**, 104, 056101.
 [20] S. Akamatsu, S. Bottin-Rousseau, G. Faivre, E. A. Brener, *Phys. Rev. Lett.* **2014**, 112, 105502.
 [21] M. Kellner, J. Hötzer, E. Schoof, B. Nestler, *Acta Mater.* **2020**, 182, 267.
 [22] M. Kellner, *PhD Thesis*, Karlsruher Institut für Technologie, **2020**.
 [23] E. Schoof, D. Schneider, N. Streichhan, T. Mittnacht, M. Selzer, B. Nestler, *Int. J. Solids Struct.* **2018**, 134, 181.
 [24] B. Böttger, J. Eiken, I. Steinbach, *Acta Mater.* **2006**, 54, 2697.
 [25] B. Nestler, A. Wheeler, *Phys. D Nonlinear Phenom.* **2000**, 138, 114.
 [26] F. Podmaniczky, G. I. Tóth, T. Pusztai, L. Gránásy, *J. Indian Inst. Sci.* **2016**, 96, 161.
 [27] F. Hinrichs, M. Kellner, J. Hötzer, B. Nestler, *Scr. Mater.* **2020**, 186, 89.
 [28] M. Kellner, M. Seiz, B. Nestler, in *High Performance Computing in Science and Engineering—Garching/Munich 2022*, Leibniz Rechenzentrum, Munich, Germany **2022**, pp. 72–73.
 [29] M. Kellner, I. Sprenger, P. Steinmetz, J. Hötzer, B. Nestler, M. Heilmaier, *Comput. Mater. Sci.* **2017**, 128, 379.
 [30] J. Peng, P. Franke, H. J. Seifert, *J. Phase Equilib. Diffus.* **2016**, 37, 592.
 [31] K. D. Noubary, M. Kellner, J. Hötzer, M. Seiz, H. J. Seifert, B. Nestler, *J. Mater. Sci.* **2021**, 56, 11932.
 [32] P. Steinmetz, M. Kellner, J. Hötzer, A. Dennstedt, B. Nestler, *Comput. Mater. Sci.* **2016**, 121, 6.
 [33] M. Kellner, S. N. Enugala, B. Nestler, *Comput. Mater. Sci.* **2022**, 203, 111046.
 [34] SuperMUC-NG, <https://doku.lrz.de/display/PUBLIC/SuperMUC-NG> (accessed: November 2022).
 [35] J. Hötzer, A. Reiter, H. Hierl, P. Steinmetz, M. Selzer, B. Nestler, *J. Comput. Sci.* **2018**, 26, 1.
 [36] Software package Parallel Algorithms for Crystal Evolution in 3D—Pace3D, <https://www.h-ka.de/en/idm/profile/pace3d-software> (Accessed: November 2022).
 [37] M. Plapp, *Phys. Rev. E* **2011**, 84, 031601.
 [38] A. Choudhury, B. Nestler, *Phys. Rev. E* **2012**, 85, 021602.
 [39] J. Hötzer, M. Jainta, P. Steinmetz, B. Nestler, A. Dennstedt, A. Genau, M. Bauer, H. Köstler, U. Råde, *Acta Mater.* **2015**, 93, 194.
 [40] B. Nestler, H. Garcke, B. Stinner, *Phys. Rev. E* **2005**, 71, 041609.
 [41] A. Karma, *Phys. Rev. Lett.* **2001**, 87, 115701.
 [42] B. Echebarria, R. Folch, A. Karma, M. Plapp, *Phys. Rev. E* **2004**, 70, 061604.
 [43] M. Kellner, W. Kunz, P. Steinmetz, J. Hötzer, B. Nestler, *Comput. Mater. Sci.* **2018**, 145, 291.
 [44] P. Steinmetz, J. Hötzer, M. Kellner, A. Dennstedt, B. Nestler, *Comput. Mater. Sci.* **2016**, 117, 205.
 [45] A. Vondrous, M. Selzer, J. Hötzer, B. Nestler, *Int. J. High Perform. Comput. Appl.* **2014**, 28, 61.
 [46] P. Steinmetz, Y. C. Yabansu, J. Hötzer, M. Jainta, B. Nestler, S. R. Kalidindi, *Acta Mater.* **2016**, 103, 192.
 [47] M. Bauer, J. Hötzer, M. Jainta, P. Steinmetz, M. Berghoff, F. Schornbaum, C. Godenschwager, H. Köstler, B. Nestler, U. Råde, in *Massively Parallel Phase-Field Simulations for Ternary Eutectic Directional Solidification*, IEEE, Austin, TX **2015**, p. 8.
 [48] C. Lomont, *Tech-315 Nical Rep.* **2003**, 32, 1.
 [49] N. Dupin, I. Ansara, B. Sundman, *Calphad Comput. Coupling Ph. Diagr. Thermochem.* **2001**, 25, 279.
 [50] J.-O. Andersson, T. Helander, L. Höglund, P. Shi, B. Sundman, *Calphad: Comput. Coupling Ph. Diagr. Thermochem.* **2002**, 26, 273.
 [51] S. Beucher, in *Proc. of the Inter. Workshop on Image Processing*, CCETT, Fontainebleau, France **1979**, pp. 17–21.
 [52] R. Barnes, C. Lehman, D. Mulla, *Comput. Geosci.* **2014**, 62, 117.
 [53] S. Beucher, F. Meyer, *Mathematical Morphology In Image Processing*, CRC Press, Boca Raton **2018**, pp. 433–481.